http://dx.doi.org/10.1016/j.jallcom.2019.153479

Orientation relationships between nanotwins inside A–B type variant pair in Ni-Mn-Ga alloy

Sheng Ouyang[a,b,1], Guangming Zhao[c,d,1], Ming Han[d], Ye Zhu[c,*], Yanqing Yang[b,*]

[a] Key Laboratory for Microstructural Control of Metallic Materials of Jiangxi Province, Nanchang Hangkong University, Jiangxi 330063, China

[b] State Key Laboratory of Solidification Processing, Northwestern Polytechnical University, Xi'an 710072, China.

[c] Department of Applied Physics, The Hong Kong Polytechnic University, Hung Hom, Kowloon, Hong Kong, China

[d] School of Materials Science and Engineering, East China Jiaotong University, Nanchang 330013, Jiangxi, China

Abstract

Microstructure of the martensitic variant pairs in Ni-Mn-Ga magnetic shape memory alloys underpins future research and development on the alloys with a large magnetic-field-induced strain. However, a complete description of the microstructure and crystallography of all variant pairs (including A–B, A–C, and A–D types) are unavailable now, because those of the A–B type are still far from being thoroughly determined. By investigating a non-modulated $Ni_{54}Mn_{25}Ga_{21}$ alloy, this paper systematically determines the orientation relationships between the nanoscale lamellae inside all three variant pairs with special emphasis on the A–B type. The microstructure

---

[1] These authors contributed equally to this work.

[*] Corresponding authors. *E-mail addresses:* yezhu@polyu.edu.hk (Ye Zhu), yqyang@nwpu.edu.cn (Yanqing Yang)

and crystallography of both perfect and imperfect nanotwins are characterized in detail. In order to fully understand the hierarchically twined microstructure, a geometric model with different variant pairs integrated together is established, by which the formation mechanism, twinning system, and deformation paths of each variant pair are explained.

Keywords: Ni-Mn-Ga alloy; A–B variant pair; Orientation relationship; Twinning; Nanotwins

1. Introduction

Ni-Mn-Ga magnetic shape memory alloys (MSMAs) capable of exhibiting a large strain and fast response when applying a moderate magnetic field have potential applications in actuators and sensors [1, 2]. The magnetic-field-induced strain (MFIS) of five-layer and seven-layer modulated structures can reach 7% and 10%, respectively [3, 4], and that of the non-modulated (NM) structure can reach as high as 12% [5]. Compared to the modulated structures, the NM one has many advantages, such as a higher performance in thermostability, ductility, and MFIS, which makes the latter more promising for practical applications [6, 7]. Since the MFIS in NM Ni-Mn-Ga MSMAs is realized by reorientation of twinned martensites with motion of twinning interfaces, understanding the microstructure and crystallography of martensites is the key to the alloys' MFIS improvement.

The microstructure of Ni-Mn-Ga MSMAs directly results from martensitic phase transformation. A single crystal of the parent phase (austenite) can transform into at most 24 variants of martensites. To minimize the shape change caused by the transformation, the martensitic variants will distribute in a self-accommodated manner.

http://dx.doi.org/10.1016/j.jallcom.2019.153479

The microstructure of the self-accommodated NM martensites is considered to be hierarchical twins, where higher-order nanotwins form inside lower-order microtwins [8, 9]. In more detail, the 24 martensitic variants are divided into six plate groups. Each group comprises four mutually twin-related variants which are arbitrarily designated as A, B, C, and D (e.g., the geometry of a (1 0 1) plate group is displayed in Fig. S1). To better describe the crystallography of the above four mutually twin-related variants, they are further categorized into three types of martensitic variant pairs, namely, A–B (or equivalently C–D), A–C (or B–D) and A–D (or B–C) [10]. Inside an individual NM martensitic variant, its substructure is nanotwins. The volume fraction of the narrower twin domains in a variant is defined as λ (Fig. S1), and its value ranges from 0 to 0.5. If no residual stress remains after the rapid martensitic transformation, the hierarchically twinned microstructure of martensites would have a fixed value of λ (which can be calculated based on a geometrically nonlinear theory of the martensitic transformation [11, 12]). In reality, however, the residual stress is inevitable, which will induce twinning/detwinning inside the martensitic variants, resulting in the variation of λ at different regions of the alloys. The twinning systems with such a hierarchically twinned microstructure are still ambiguous up to now. For that reason, many reported deformation behaviors of the NM martensites cannot be comprehended satisfactorily [13-18]. Therefore, a complete description of the microstructure and crystallography of all variant pairs (including A–B, A–C, and A–D types) in a plate group is indispensable for future research and development in MSMAs.

http://dx.doi.org/10.1016/j.jallcom.2019.153479

Many efforts have been made to investigate the crystallography of the NM Ni-Mn-Ga alloys, from their martensitic transformation to their nanotwin substructure. Chulist et al. studied the orientation relationships (ORs) between the parent austenite and the martensitic variants, and showed that the OR was not strictly fixed but depended on the type and width of the martensitic variants [19]. Pond et al. described the internal twinning process in an individual martensitic variant and revealed the microscopic formation mechanism of the nanotwins [20]. Cong, Zuo and their co-workers reported that the ORs between nanotwins across the interfaces of variant pairs generally deviated by a few degrees from either a perfect twin relationship or an identical orientation [21-23]. With respect to specific variant pairs, Muntifering et al. investigated the A–D type [24, 25], and Ouyang et al. focused on the A–C type [26, 27]. Although the detailed crystallography of the martensitic variant pairs A–D and A–C are quite different, generally the ORs between the variants in both types can be expressed as rotations around a common lattice direction. The rotation angles are mainly decided by the crucial parameter λ.

Currently, the crystallography of the A–B type martensitic variant pair is far from being thoroughly understood. This is partly due to the fact that it is challenging to find a common lattice direction along which the nanotwin boundaries inside both variants A and B are edge-on oriented, leading to the inconvenience caused when measuring the crucial parameter λ for both variants. As a consequence, a comprehensive study of all variant pairs (A–B, A–C, and A–D) which includes their microstructures and ORs in a plate group remains unavailable until now.

http://dx.doi.org/10.1016/j.jallcom.2019.153479

In the present work, we first mainly focus on determination of the ORs between the nanotwins inside A–B type variant pair by transmission electron microscopy (TEM). The experimental observations are supported by theoretical calculation according to the geometrically nonlinear theory of martensitic transformation. We also perform similar experimental and theoretical analysis of both A–C and A–D type variant pairs. By integrating all obtained results about the three variant pairs, we build a geometric model for a whole NM martensitic plate group, which clarifies the twinning systems of its hierarchical twins. Finally, based on this geometric model, we illustrate the development of the hierarchically twinned microstructure by describing the formation mechanisms that underlie different variant pairs, and further proposed a detailed explanation of the possible deformation paths in an NM martensitic plate group.

2. Experimental

A button ingot with a nominal composition of $Ni_{54}Mn_{25}Ga_{21}$ is prepared from the constitutive metals (Ni of 99.99%, Mn of 99.97% and Ga of 99.999% purity) in an induction melting furnace under argon atmosphere and cast into a steel mold. Since the martensitic transformation finish temperature (M_f) of this alloy is about 100 °C, the parent phase austenite completely transforms into martensite at room temperature. The austenite has a cubic $L2_1$ structure ($a_A = 0.5840$ nm) [28], and the NM martensitic phase is a tetragonal $L1_0$ structure ($a_M = 0.3780$ nm, $c_M= 0.6827$ nm) [29]. TEM samples are prepared through the processes of slicing, mechanical grinding and punching into 3 mm TEM discs about 80 μm thick. The central portions of the discs are further reduced to about 10 μm by mechanical dimpling followed by polishing. Final perforation of the

TEM samples is conducted via precision argon ion milling using Gatan 691 PIPS machine operated at an acceleration voltage of 5 kV. High resolution TEM (HRTEM) observation is carried out on a Tecnai F30 G^2 electron microscope operated at 300 kV. The rotation between bright field (BF) images and corresponding selected area electron diffraction (SAED) patterns is carefully calibrated.

3. Results

3.1. TEM observations on the A–B type variant pair

As shown in Fig. S1, the ORs between the nanoscale lamellae in any variant pair have two categories, namely, twin relationship of the inner-variant nanotwins, and ORs between the inter-variant lamellae. The former was determined to be a compound type [20, 29, 30]. The latter is identified in the following.

3.1.1. Morphology and inner-variant microstructure

Fig. 1a is a BF image of the self-accommodated NM martensitic variants in a plate group. The four types of martensitic variants (A, B, C, D) have different orientations. Typical inter-variant interfaces are traced with dashed lines. It is clear in Fig. 1a that the trace of the A–B interface slightly deviates from the A–C interface and is nearly perpendicular to that of the A–D (or B–C). Different variant pairs have distinct morphologies, namely, wedge-like (A–B), spear-like (A–C), and fork-like (A–D or B–C). For a clear illustration, these featured shapes are sketched in Fig. 1b.

For each individual variant, its width is about 0.5 μm. It is further composed of two lamellae: the wider major lamella and the narrower minor lamella, as shown in Fig. 1c (a magnified image of the marked frame in Fig. 1a). A pair of major and minor lamellae

http://dx.doi.org/10.1016/j.jallcom.2019.153479

has a width of about 10 nm. The SAED pattern in Fig. 1c shows a coincidence of the 1 1 2 diffraction spots from different lamellae, confirming that the major–minor lamellar pairs inside a variant are nanotwins. Their twinning elements are identified to be: the twinning plane $K_1 = \{1\ 1\ 2\}$, the twinning direction $\eta_1 = \langle 1\ 1\ \bar{1} \rangle$, the second undistorted plane $K_2 = \{\bar{1}\ \bar{1}\ 2\}$, the conjugate twinning direction $\eta_2 = \langle 1\ 1\ 1 \rangle$, and the magnitude of shear $s = 0.4941$.

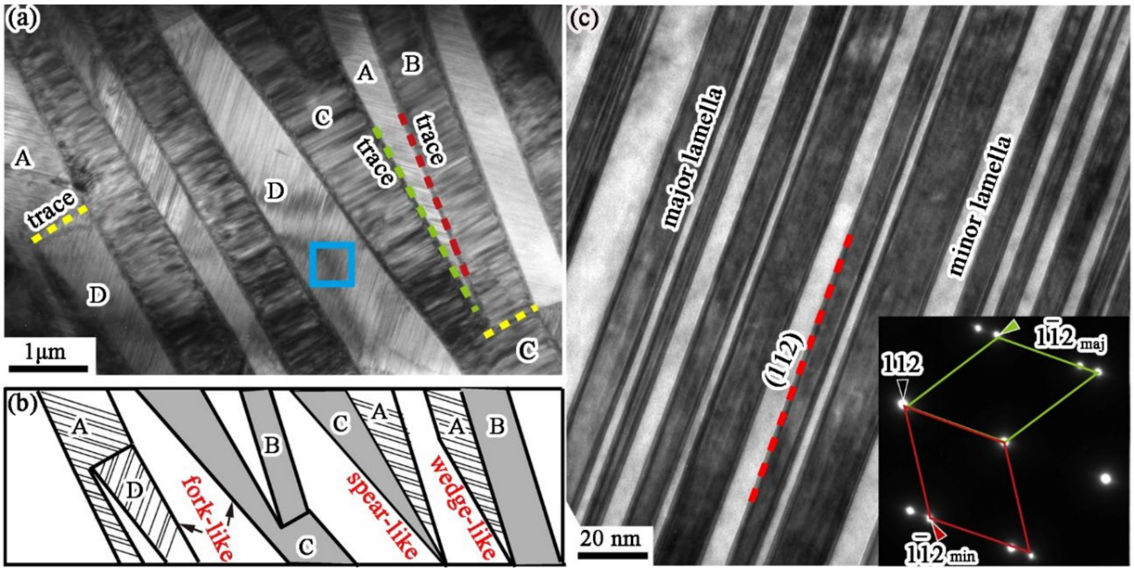

Fig. 1. NM martensitic variants in a plate group: (a) A BF image showing the morphology of self-accommodated martensites; (b) A schematic of the wedge-, spear- and fork-like shapes. (c) Enlargement of the blue frame region in (a). The inset is an SAED pattern taken along the $[\bar{2}\ 0\ 1]_{maj}$ // $[2\ 0\ \bar{1}]_{min}$ zone axis.

http://dx.doi.org/10.1016/j.jallcom.2019.153479

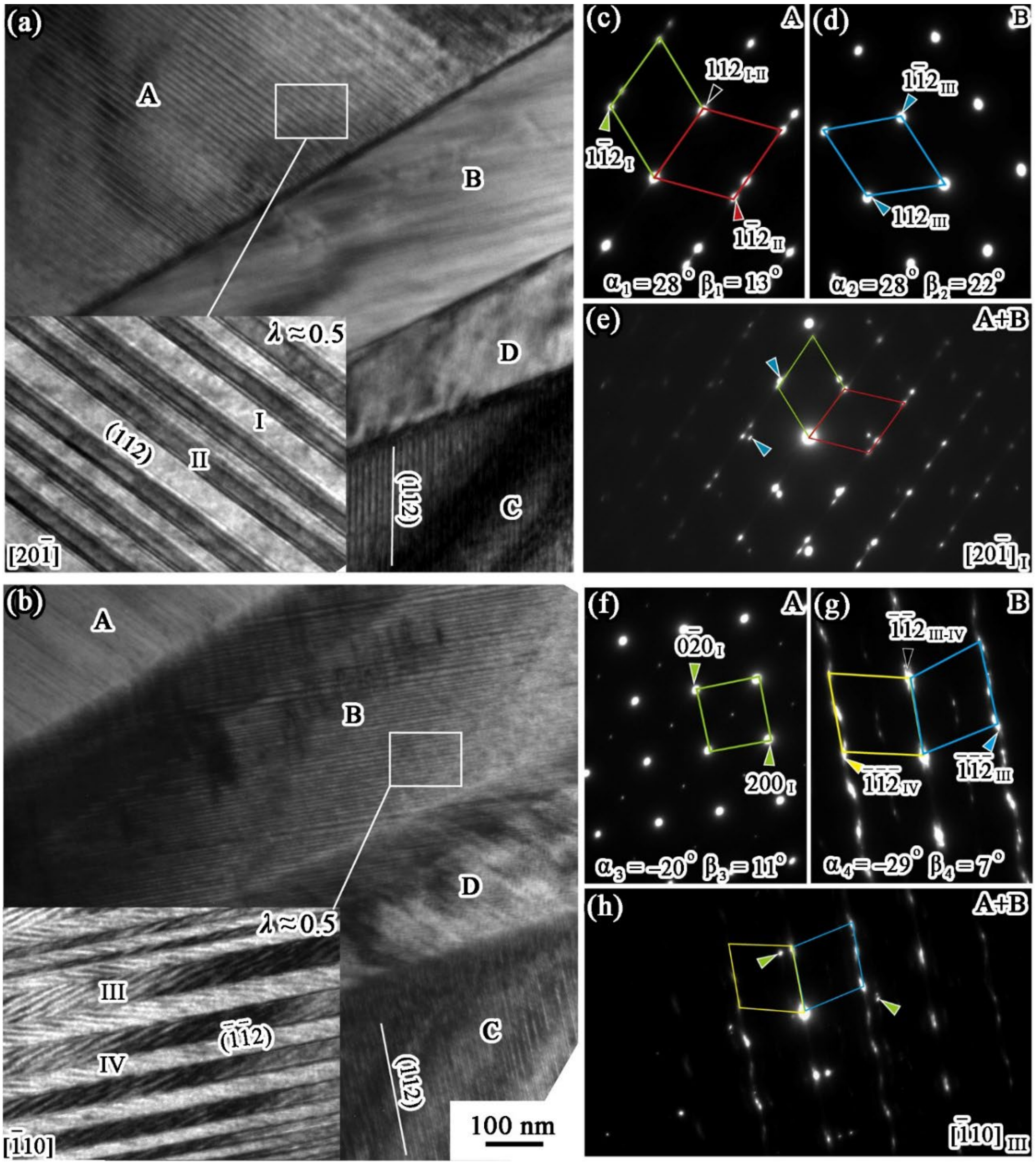

Fig. 2. Microstructural configuration of the variant pair A–B with λ ≈ 0.5. (a–b) BF images of A–B. (c–h) SAED patterns taken from the variant A (c, f), the variant B (d, g) and the variant pair A–B (e, h). The viewing directions are $[2\ 0\ \bar{1}]_{\mathrm{I}}$ (c, e), $[\bar{2}\ 0\ 1]_{\mathrm{III}}$ (d), $[0\ 0\ \bar{1}]_{\mathrm{I}}$ (f), and $[\bar{1}\ 1\ 0]_{\mathrm{III}}$ (g, h).

3.1.2. ORs between inter-variant lamellae

Fig. 2a displays a microstructural configuration of the variant pair A–B with $\lambda \approx 0.5$. Inside the variant A, the major and minor lamellae are denoted as I and II, respectively. Inside the variant B, the major and minor lamellae are III and IV, respectively. Viewed along the $[2\ 0\ \bar{1}]$ direction of the lamella I, the nanotwin boundaries inside variant A are edge-on, as shown in Fig. 2a. The edge-on condition for variant B is $[\bar{1}\ 1\ 0]$ direction of the lamella III, as shown in Fig. 2b. Inside each single variant, the major–minor lamellar pairs are $\{1\ 1\ 2\}$ nanotwins (refer to Section 3.1.1). From the four crystallographically equivalent $\{1\ 1\ 2\}$ lattice planes, $(1\ 1\ 2)$ is assigned to be the twinning plane of the nanotwins inside variants A and C, and $(\bar{1}\ \bar{1}\ 2)$ corresponds to that inside the variants B and D.

The ORs between inter-variant lamellae across the A–B interface comprise three components, i.e., OR between the major–major lamellae I–III, OR between the minor–minor lamellae II–IV, and OR between the major–minor lamellae I–IV (or II–III). These three ORs are mutually dependent. If any one of them were determined, the other two ORs can be deduced based on the already determined nanotwin relationship inside an individual variant. Here we will determine the OR between the lamellae I–III first. Then in the next section the ORs between the lamellar pairs II–IV, I–IV are calculated by means of the already determined ORs.

Figs. 2c–2h show a series of SAED patterns. Figs. 2c and 2f are both taken from the variant A. These two patterns are along the $[2\ 0\ \bar{1}]_{\mathrm{I}}$ and $[0\ 0\ \bar{1}]_{\mathrm{I}}$ zone axes, respectively. The subscript (I) denotes lamella I. Figs. 2d and 2g are taken from the variant B along its $[\bar{2}\ 0\ 1]_{\mathrm{III}}$ and $[\bar{1}\ 1\ 0]_{\mathrm{III}}$ zone axes, respectively. The directions $[2\ 0\ \bar{1}]_{\mathrm{I}}$ and $[\bar{2}\ 0\ 1]_{\mathrm{III}}$ deviate slightly from each other, and so do $[0\ 0\ \bar{1}]_{\mathrm{I}}$ and $[\bar{1}\ 1\ 0]_{\mathrm{III}}$. As a result, in the diffraction patterns taken from both variants A and B (Figs. 2e and 2h), the $[\bar{2}\ 0\ 1]_{\mathrm{III}}$ diffraction pattern (indicated by blue arrows in Fig. 2e) and the $[0\ 0\ \bar{1}]_{\mathrm{I}}$ diffraction pattern (indicated by green arrows in Fig. 2h) are still visible when the $[2\ 0\ \bar{1}]_{\mathrm{I}}$ and $[\bar{1}\ 1\ 0]_{\mathrm{III}}$ patterns appear clearly.

The misorientation angles between above zone axes are calculated as follows. In a TEM with a side-entry double-tilt holder, the orientation of a crystal is expressed by two tilt angles: α_i around the axis of the specimen holder, and β_i around an axis perpendicular to the holder. The orientation of another crystal is expressed by α_j and β_j. The misorientation angle between the two crystals, $\delta_{i\text{-}j}$, can be calculated by [31]

$$\cos\delta_{i-j} = \cos(\alpha_i - \alpha_j)\cos(\beta_i - \beta_j) \tag{1}$$

Substituting the recorded tilt angles (α_1, β_1), (α_2, β_2), (α_3, β_3), (α_4, β_4) given in Fig. 2 into the Eq. 1, two misorientation angles can be obtained:

$$\delta_{1\text{–}2}\,(\lambda = 0.5) = [2\ 0\ \bar{1}]_{\mathrm{I}} \wedge [\bar{2}\ 0\ 1]_{\mathrm{III}} \approx 9^\circ$$

$$\delta_{3\text{–}4}\,(\lambda = 0.5) = [0\ 0\ \bar{1}]_{\mathrm{I}} \wedge [\bar{1}\ 1\ 0]_{\mathrm{III}} \approx 10^\circ$$

The above two sets of zone axes and their misorientation angles represent the OR between the lamellae I–III.

http://dx.doi.org/10.1016/j.jallcom.2019.153479

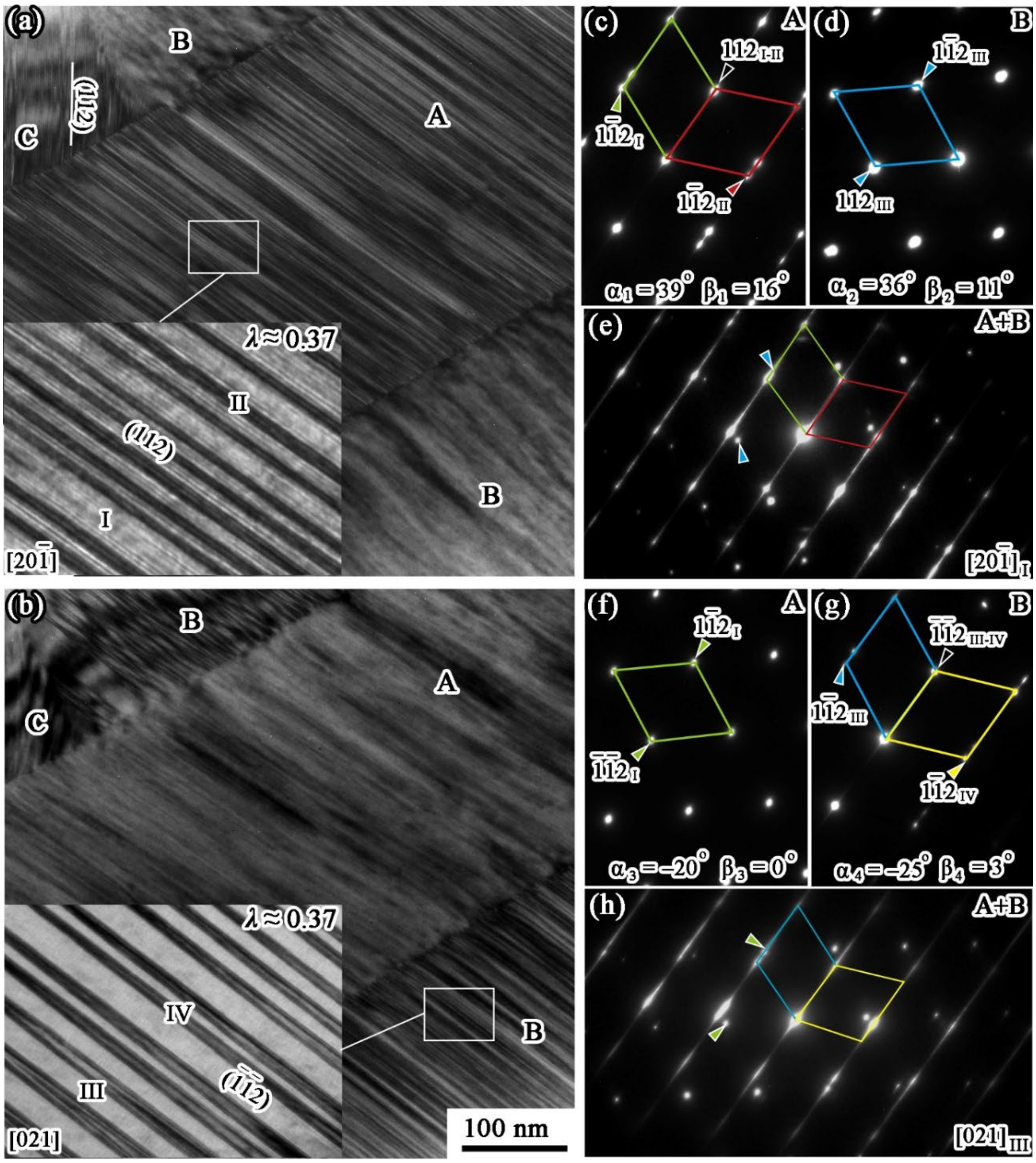

Fig. 3. Microstructural configuration of the variant pair A–B with $\lambda \approx 0.37$. (a–b) BF images of A–B. (c–h) SAED patterns captured from the variant A (c, f), the variant B (d, g) and the variant pair A–B (e, h). The viewing directions are $[2\,0\,\bar{1}]_{\mathrm{I}}$ (c, e), $[\bar{2}\,0\,1]_{\mathrm{III}}$ (d), $[0\,\bar{2}\,\bar{1}]_{\mathrm{I}}$ (f), $[0\,2\,1]_{\mathrm{III}}$ (g, h).

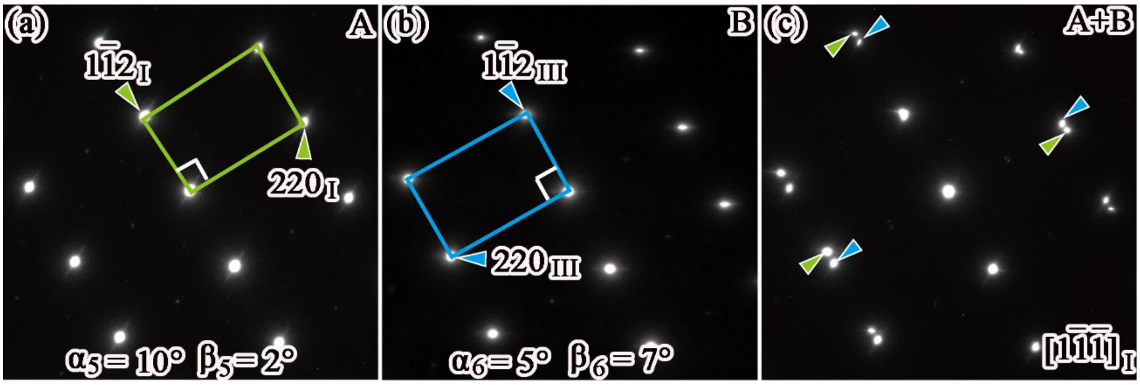

Fig. 4. SAED patterns taken from the variant A (a), the variant B (b) and the variant pair A–B (c) with $\lambda \approx 0.37$. The patterns are taken along $[1\ \bar{1}\ \bar{1}]_{\mathrm{I}}$ (a, c) and $[\bar{1}\ 1\ 1]_{\mathrm{III}}$ (b).

Fig. 3 (like Fig. 2) displays a microstructural configuration of the variant pair A–B with $\lambda \approx 0.37$. In both Figs. 3a and 3b, the nanotwin boundaries appear edge-on in either variant A or B. By analyzing the SAED patterns with corresponding tilt angles, which are collected from the variant A (Figs. 3c and 3f and Fig. 4a), the variant B (Figs. 3d and 3g and Fig. 4b), and the variant pair A–B (Figs. 3e and 3h and Fig. 4c), we obtain

$$\delta_{1\text{–}2}(\lambda = 0.37) = [2\ 0\ \bar{1}]_{\mathrm{I}} \wedge [\bar{2}\ 0\ 1]_{\mathrm{III}} \approx 6°$$

$$\delta_{3\text{–}4}(\lambda = 0.37) = [0\ \bar{2}\ \bar{1}]_{\mathrm{I}} \wedge [0\ 2\ 1]_{\mathrm{III}} \approx 6°$$

$$\delta_{5\text{–}6}(\lambda = 0.37) = [1\ \bar{1}\ \bar{1}]_{\mathrm{I}} \wedge [\bar{1}\ 1\ 1]_{\mathrm{III}} \approx 7°$$

It is clear that $\delta_{1\text{–}2}(\lambda = 0.5) \neq \delta_{1\text{–}2}(\lambda = 0.37)$, which means the ORs between the lamellae I–III for $\lambda \approx 0.5$ and 0.37 are not identical. Further analysis shows that the lamellae I–III are not $(1\ \bar{1}\ 2)$ twin related. In Fig. 4(c) several diffraction spots from the lamellae I–III deviate slightly from each other, directly showing that the $[1\ \bar{1}\ \bar{1}]_{\mathrm{I}}$ and $[\bar{1}\ 1\ 1]_{\mathrm{III}}$ zone patterns are not coincident exactly. If a perfect twin relationship exists between the two lamellae, an exact coincidence of the $[1\,\bar{1}\,\bar{1}]_{\mathrm{I}}$ and $[\bar{1}\,1\,1]_{\mathrm{III}}$ zone patterns should be observed.

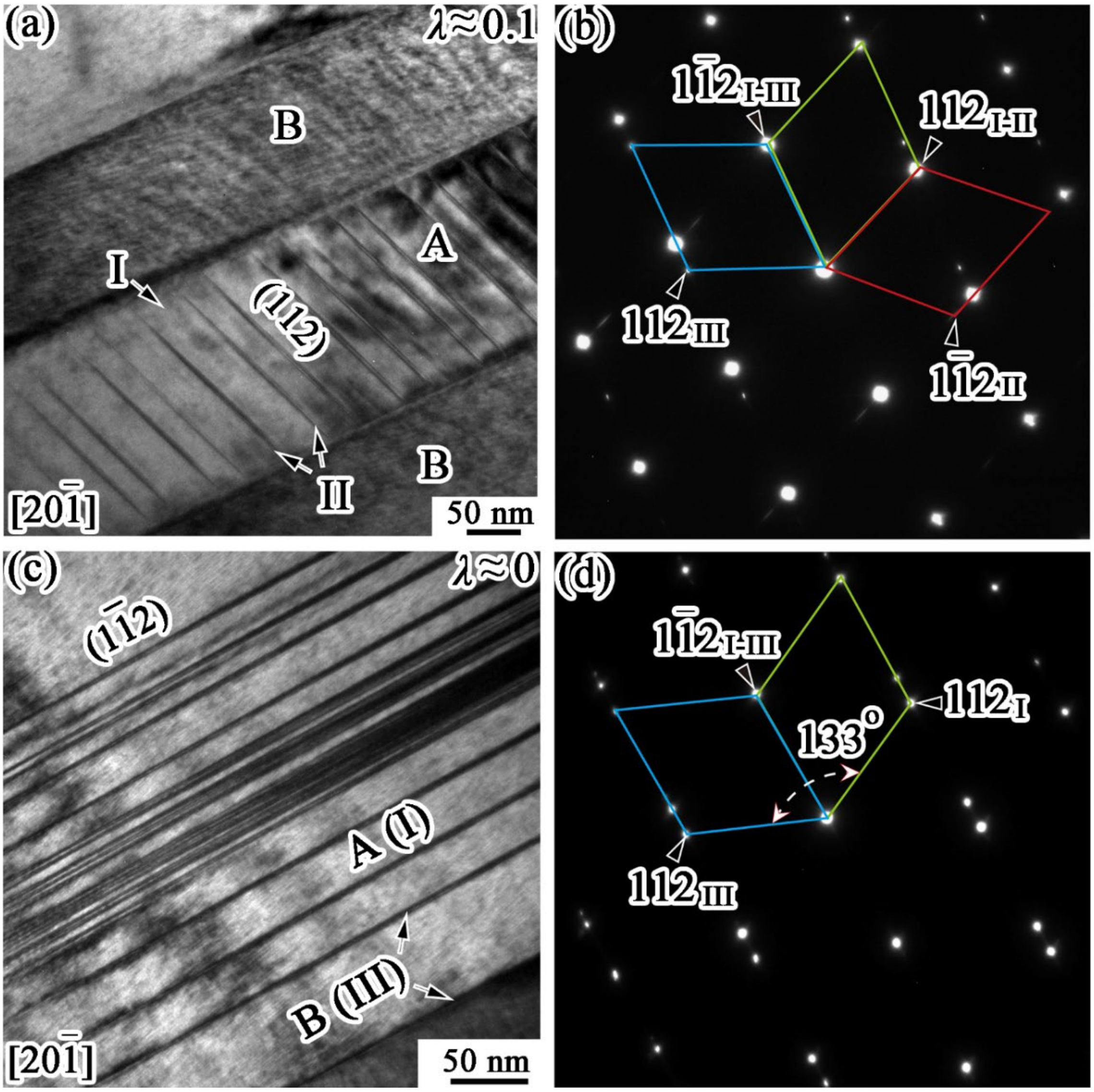

Fig. 5. BF images and SAED patterns of the variant pair A–B with $\lambda \approx 0.1$ (a, b) and 0 (c, d). The viewing direction is $[2\,0\,\bar{1}]_{\mathrm{I}} \,//\, [\bar{2}\,0\,1]_{\mathrm{III}}$.

For $\lambda \approx 0.1$, the width of the paired lamellae in a single variant increases to about 50 nm (Fig. 5a). An SAED pattern (Fig. 5b) shows that

http://dx.doi.org/10.1016/j.jallcom.2019.153479

$$[2\ 0\ \bar{1}]_{\mathrm{I}} \,//\, [\bar{2}\ 0\ 1]_{\mathrm{III}} \text{ and } (1\ \bar{1}\ 2)_{\mathrm{I}} \,//\, (1\ \bar{1}\ 2)_{\mathrm{III}}$$

Within an experimental error about 2°, the lamellae I–III are identified to be a $(1\ \bar{1}\ 2)$ twin. For $\lambda \approx 0$, the major lamella I (or III) becomes the variant A (or B), as shown in Fig. 5c, and the lamellae I–III still maintain a twin relation (Fig. 5d).

Our experimental observations reveal that the OR between the inter-variant major–major lamellae varies with λ: for large λ (e.g. 0.5 and 0.37) it is close to a $(1\ \bar{1}\ 2)$ twin relationship; for small λ (e.g. 0.1 and 0) it exactly matches the $(1\ \bar{1}\ 2)$ twin relationship.

Furthermore, the morphology of the A–B interface also changes with λ. In Fig. 6 viewed along the $[\bar{2}\ 0\ 1]_{\mathrm{I}}$ direction, the A–B interfaces with different λ are indicated by a pair of black arrows. For large λ (about 0.5 and 0.37 in Figs. 6a–6b), the inter-variant interface (not exactly edge-on) exhibits a wavy character, while for small λ (about 0.1 and 0 in Figs. 6c–6d) it is dominated by a straight $(1\ \bar{1}\ 2)$ twin boundary, especially when $\lambda \approx 0$ the A–B interface becomes a coherent twin boundary (Fig. 6d).

http://dx.doi.org/10.1016/j.jallcom.2019.153479

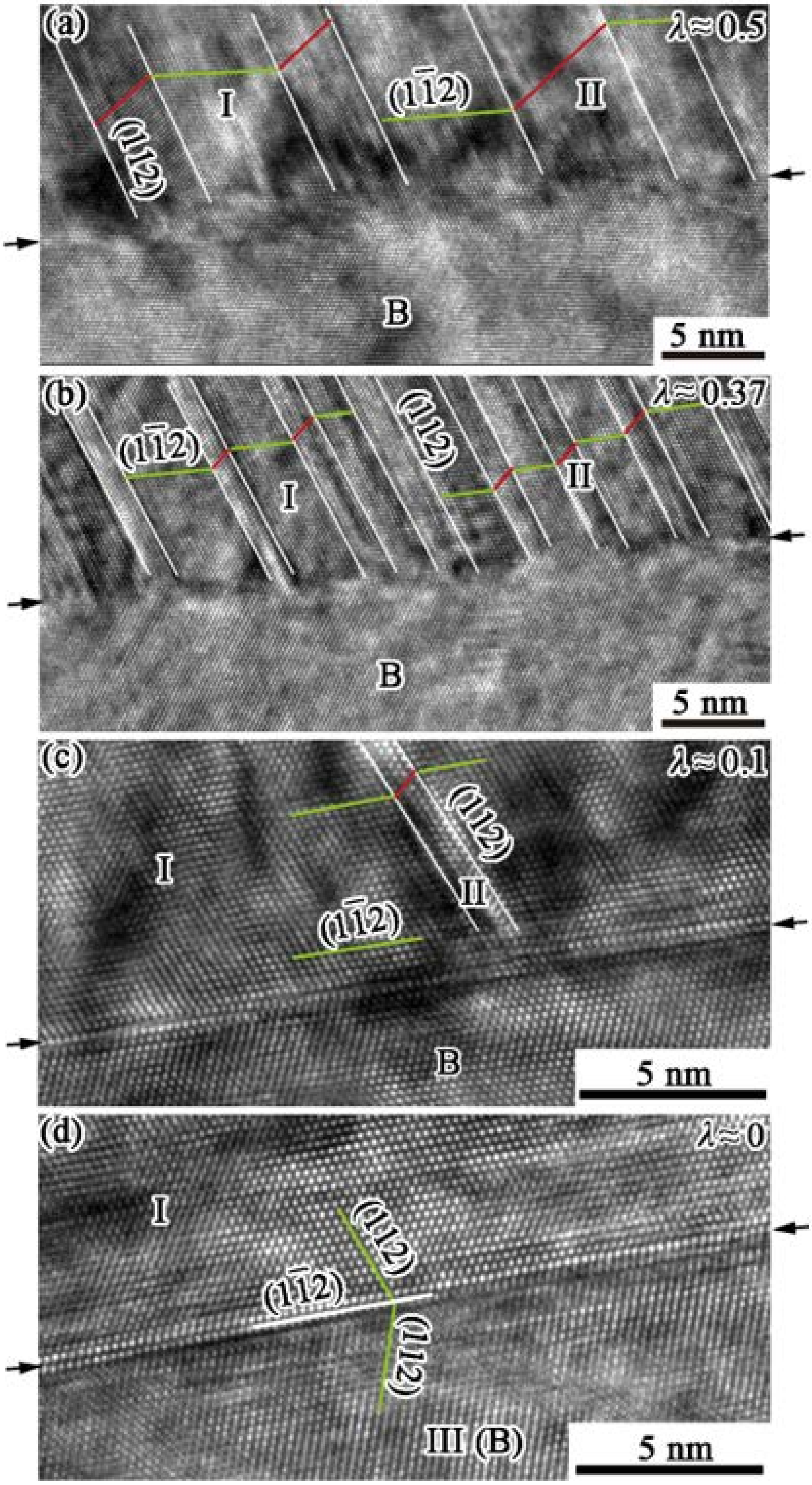

Fig. 6. HRTEM images of the A–B interfaces with different λ.

.

3.2. Theoretical calculation of the ORs

In order to confirm the above experimental results, in this section we employ the geometrically nonlinear theory of martensitic transformation to perform calculations [11, 12, 32, 33] . First of all, the OR between the variants A and B (in both of which there are nanoscale lamellae) needs to be specified. In the supplementary material (Section 1), the variant pair A–B is predicted to be a type II twin (i.e., rational K_2 and η_1).

Secondly, the OR between a variant and its internal lamellae needs to be clarified too. The OR between a variant and its internal major lamella can be expressed by a rotation matrix **R**

$$\mathbf{R} = \mathbf{C}\ \mathbf{S}^{*-1} \tag{2}$$

where **C** is the lattice correspondence between variant and lamella; $\mathbf{S}^*$ is an average twinning shear; the superscript –1 denotes an inverse matrix. The twinning shear $\mathbf{S}^*$ is a function of λ

$$\mathbf{S}^* = \mathbf{I} + (\lambda s)\hat{\mathbf{a}}\hat{\mathbf{n}}^{\mathrm{T}} \tag{3}$$

where $\hat{\mathbf{n}}$ is a unit vector normal to the {1 1 2} twinning plane; $\hat{\mathbf{a}}$ is a unit vector parallel to the <1 1 $\bar{1}$> twinning direction; the superscript T denotes matrix transposition. In the case of variant A between its internal major lamella I (i.e., A–I), $\hat{\mathbf{n}}$ is assigned to be normal to the (1 1 2) twinning plane, and **C** is equal to an identity matrix. In the case of B–III, $\hat{\mathbf{n}}$ is assigned to be normal to the ($\bar{1}$ $\bar{1}$ 2) twinning plane, and **C** denotes [1 1 $\bar{1}$]$_\mathrm{B}$

→ [1 1 1]$_{\mathrm{III}}$ and (1 1 2)$_{\mathrm{B}}$ → $(\bar{1}\ \bar{1}\ 2)_{\mathrm{III}}$. Hence, the ORs between a variant (A or B) and its major lamella (I or III) are:

$$\mathbf{R}_{\mathrm{A-I}} = \mathbf{S}^{*-1}_{(112)},\ \mathbf{R}_{\mathrm{B-III}} = \mathbf{C}_{\mathrm{B-III}}\mathbf{S}^{*-1}_{(\bar{1}\bar{1}2)} \tag{4}$$

For more details, this issue was studied in our previous work [26].

Finally, the ORs between the lamellae inside variant pair A–B can be deduced. According to Eq. S2 and Fig. S1, the twin relationships of the inner-variant lamellae I–II (in variant A) and III–IV (in variant B) are calculated to be

$$\mathbf{R}^{(112)}_{\mathrm{I-II}} = \begin{pmatrix} -0.3801 & 0.6199 & 1.2398 \\ 0.6199 & -0.3901 & 1.2398 \\ 0.3801 & 0.3801 & -0.2398 \end{pmatrix},\quad \mathbf{R}^{(\bar{1}\bar{1}2)}_{\mathrm{III-IV}} = \begin{pmatrix} -0.3801 & 0.6199 & -1.2398 \\ 0.6199 & -0.3901 & -1.2398 \\ -0.3801 & -0.3801 & -0.2398 \end{pmatrix} \tag{5}$$

Combining the already calculated rotation matrices, $\mathbf{R}_{\mathrm{A-B}}$, $\mathbf{R}_{\mathrm{A-I}}$, $\mathbf{R}_{\mathrm{B-III}}$, $R_{\mathrm{I-II}}$, $\mathbf{R}_{\mathrm{III-IV}}$ (Eq. S10 and Eqs. 4–5), the ORs between inter-variant lamellae across the A–B interface are:

- For major–major lamellae I–III, $\mathbf{R}_{\mathrm{I-III}} = \left[\mathbf{S}^{*}_{(112)}\right]\mathbf{R}_{\mathrm{A-B}}\left[\mathbf{C}_{\mathrm{B-III}}\mathbf{S}^{*-1}_{(\bar{1}\bar{1}2)}\right]$
- For minor–minor lamellae II–IV, $\mathbf{R}_{\mathrm{II-IV}} = \mathbf{R}_{\mathrm{I-II}}\mathbf{R}_{\mathrm{I-III}}\mathbf{R}_{\mathrm{III-IV}}$
- For major–minor lamellae I–IV (or II–III), $\mathbf{R}_{\mathrm{I-IV}} = \mathbf{R}_{\mathrm{I-III}}\mathbf{R}_{\mathrm{III-IV}}\left(\text{or } \mathbf{R}_{\mathrm{II-III}} = \mathbf{R}_{\mathrm{I-II}}\mathbf{R}_{\mathrm{I-III}}\right)$

Above rotation matrices for the inter-variant lamellar pairs across the A–B interface vary with λ, which are summarized in Table 1. The meaning of each quantitative 3×3 matrix in this table is decoded by a series of rotational operations (also explained in Table 1).

The theoretically calculated ORs between inter-variant lamellae across the A–B interface are compared with experimental ones. The angle δ is a key parameter describing the experimentally recorded ORs (Eq. 1). In Table 2 and Fig. S4a, the theoretical values of δ (calculated according to the rotation matrices in Table 1) are in general agreement with the experimental ones.

Table 2. Experimental and theoretical misorientation angle δ between two lamellae with different values of λ.

λ	δ	**Experimental**	**Theoretical**
0.5	$\delta_{1\text{–}2} = [2\ 0\ \bar{1}]_{\mathrm{I}} \wedge [\bar{2}\ 0\ 1]_{\mathrm{III}}$ $[\bar{2}\ 0\ 1]_{\mathrm{II}} \wedge [\bar{2}\ 0\ 1]_{\mathrm{III}}$	9° ± 2°	11.0°
	$\delta_{3\text{–}4} = [0\ 0\ \bar{1}]_{\mathrm{I}} \wedge [\bar{1}\ 1\ 0]_{\mathrm{III}}$ $[0\ 0\ \bar{1}]_{\mathrm{I}} \wedge [1\ \bar{1}\ 0]_{\mathrm{IV}}$	10° ± 2°	9.2°
0.37	$\delta_{1\text{–}2} = [2\ 0\ \bar{1}]_{\mathrm{I}} \wedge [\bar{2}\ 0\ 1]_{\mathrm{III}}$ $[\bar{2}\ 0\ 1]_{\mathrm{II}} \wedge [\bar{2}\ 0\ 1]_{\mathrm{III}}$	6° ± 2°	8.0°
	$\delta_{3\text{–}4} = [0\ \bar{2}\ \bar{1}]_{\mathrm{I}} \wedge [0\ 2\ 1]_{\mathrm{III}}$ $[0\ \bar{2}\ \bar{1}]_{\mathrm{I}} \wedge [0\ \bar{2}\ \bar{1}]_{\mathrm{IV}}$	6° ± 2°	8.0°
	$\delta_{1\text{–}4} = [2\ 0\ \bar{1}]_{\mathrm{I}} \wedge [0\ \bar{2}\ \bar{1}]_{\mathrm{III}}$	65° ± 2°	70.2°
	$\delta_{5\text{–}6} = [1\ \bar{1}\ \bar{1}]_{\mathrm{I}} \wedge [\bar{1}\ 1\ 1]_{\mathrm{III}}$	7° ± 2°	8.5°
0.1	$\delta_{1\text{–}2} = [2\ 0\ \bar{1}]_{\mathrm{I}} \wedge [\bar{2}\ 0\ 1]_{\mathrm{III}}$ $[\bar{2}\ 0\ 1]_{\mathrm{II}} \wedge [\bar{2}\ 0\ 1]_{\mathrm{III}}$	0° ± 2°	2.1°
0	$\delta_{1\text{–}2} = [2\ 0\ \bar{1}]_{\mathrm{I}} \wedge [\bar{2}\ 0\ 1]_{\mathrm{III}}$	0° ± 2°	0°
	$\delta_{1\text{–}4} = [2\ 0\ \bar{1}]_{\mathrm{I}} \wedge [0\ \bar{2}\ \bar{1}]_{\mathrm{I\,(III)}}$	60° ± 2°	63.3°

Moreover, we also perform similar calculations to predict the ORs between inter-variant lamellae across the A–C and B–C (or A–D) interfaces (Tables S4–S5). After analyzing the variant pairs A–C (Fig. S2) and B–C (Fig. S3) and their constitutive lamellae, good agreements between theory and experiments are obtained too, as demonstrated in Fig. S4b. More details about the analysis of the variant pairs A–C and B–C are given in the supplementary material (Section 2).

Owing to above good agreements achieved, the ORs between all inter-variant lamellae across the A–B, A–C, and A–D (or B–C) interfaces are confirmed. This allows, therefore, the crystallography of all lamellae in a plate group of NM Ni-Mn-Ga alloy to be unveiled, as summarized below:

i. a simple rotation (< 25°) without {1 1 2} twin relationship.

ii. $(1\ \bar{1}\ 2)$ twinning operation plus a small (< 12°) rotation, with the twinning plane nearly parallel to the inter-variant interface.

iii. $(1\ 1\ 2)$ or $(\bar{1}\ \bar{1}\ 2)$ twinning operation plus a rotation (< 25°), with the twinning plane exactly parallel to the inner-variant nanotwin boundary.

For all major–major, minor–minor, and major–minor lamellae in the variant pairs A–B (Figs. 2–6), A–C (Fig. S2), and A–D (or B–C, Fig. S3) of an NM martensitic plate group, their ORs can be classified into one of the above three crystallographic characteristics (Table 3).

From the above microstructural and crystallographic results of all nanoscale lamellae in the variants A, B, C, and D, a geometric model illustrating the configuration of a martensitic plate group in NM Ni-Mn-Ga alloy can be constructed next.

Table 3. Classification of the ORs between all lamellae across the A–B, A–C, and A–D (or B–C) inter-variant interfaces.

Lamellar pair	**A–B**	**A–C**	**A–D / B–C**
major–major	**ii**	**ii**	**i**
minor–minor	**i**	**i**	**i**
major–minor	**iii**	**iii**	**iii**

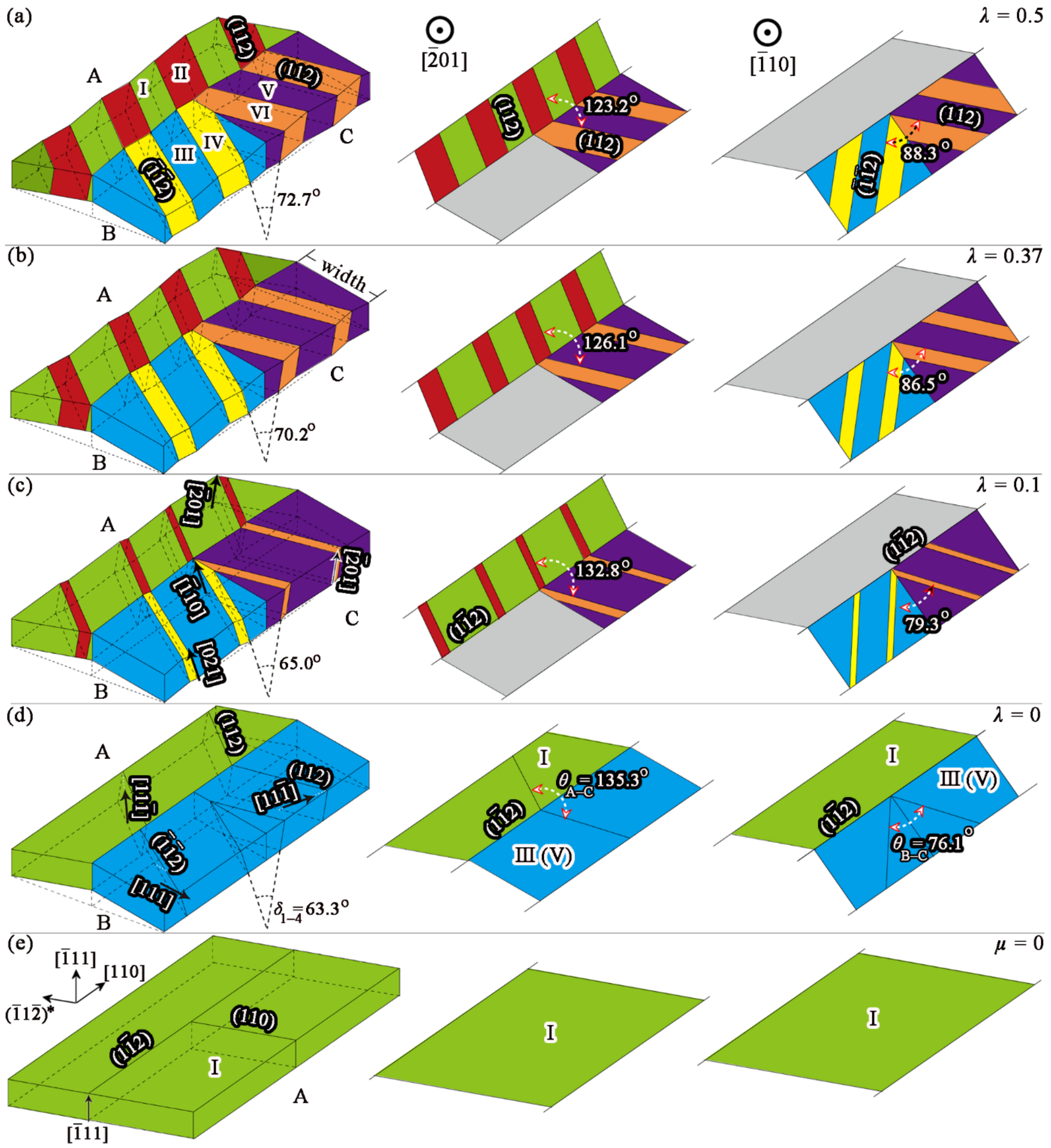

Fig. 7. A geometric model illustrating the microstructural configurations of an NM martensitic plate group when λ = 0.5 (a), 0.37 (b), 0.1 (d), 0 (d) and μ = 0 (e). The marked angles are theoretical values.

4. Discussion

4.1. A geometric model of an NM martensitic plate group

Although there are four martensitic variants existing in a plate group, only three types of variant pairs, namely, A–B, A–C, and B–C (or A–D) with distinctive ORs are formed. For clearly illustrating the microstructure and crystallography of a plate group, we only use these three variants A, B, and C to draw the geometric model.

The left column of Fig. 7 schematically shows the microstructural configurations of a plate group with decreasing values of λ (marked in each row of this figure). The middle column displays a projection view along the $[\bar{2}\ 0\ 1]$ direction corresponding to each λ, and similarly the right column is a $[\bar{1}\ 1\ 0]$ projection of the left column. In Fig. 7a, the variant A is comprised of two lamellae: I (green) and II (red), assuming I is the major lamella and II the minor one. In variant B, III (blue) is the major lamella and IV (yellow) the minor one. In variant C, V (purple) and VI (orange) are the major and minor lamellae, respectively.

The crystallography of above six lamellae in a martensitic plate group are also embodied in Fig. 7. In the left part of Fig. 7a, the lamellae I–II in variant A are nanotwins, with the (1 1 2) plane being their twin boundary. In variant B, III–IV are nanotwins with the $(\bar{1}\ \bar{1}\ 2)$ twin boundary. In variant C, V–VI are nanotwins with the (1 1 2) twin boundary, which is very similar to the lamellae I–II in variant A. If viewed along the $[\bar{2}\ 0\ 1]$ direction, the twin boundaries in variant pair A–C are at edge-on position, and if viewed along the $[\bar{1}\ 1\ 0]$ direction, those in B–C become edge-on, as shown in the middle and right parts of Fig. 7a, respectively. Figs. 7b–7c draw the pictures of a plate group as λ decreases from 0.37 to 0.1. When λ further decreases to 0 (i.e., all minor lamellae in the three variants vanish, Fig. 7d), the major lamellae I, III, and V become identical to the variants A, B, and C, respectively. Because the inter-variant lamellae I–III and I–V are both $(1\,\bar{1}\,2)$ twin related (Table 3), the lamellae III and V (or variants B and C) have an identical orientation (and thus identical blue color in Fig. 7d). In other words, the six nanotwins in a plate group can form a microtwin as λ decreases to 0. After $\lambda = 0$, we introduce a new parameter μ[†], which means the volume fraction of the minor variant in a variant pair. When $\mu = 0$ (Fig. 7e), the microtwin (Fig. 7d) becomes a single crystal.

4.2. Application of the geometric model

4.2.1. The twinning systems in hierarchically twinned martensites

Theoretically, the ORs between inter-variant lamellae will change during a twinning process which also changes λ. By analyzing the variation of λ, the twinning systems in the hierarchically twinned martensites can be revealed. Viewed from bottom to top of the geometric model (i.e., from Figs. 7e to 7a), a plate group of NM martensites with a hierarchically twinned microstructure can be understood as originating from a single crystal, then formed by a two-step twinning process.

When $\lambda = 0$, Figs. 7e to 7d show the primary twinning which generates a microtwin A–B from a single crystal A. The system for this primary twinning (represented by K_1, η_1) corresponds to $(1\,\bar{1}\,2)[\bar{1}\,1\,1]$ (marked in Fig. 7e).

[†] λ and μ are very similar in terms of definition. The former is related the minor (thinner) lamella with nanometer thickness in a variant, while the latter is related to the minor (thinner) variant with micrometer thickness in a variant pair.

http://dx.doi.org/10.1016/j.jallcom.2019.153479

When $\lambda > 0$, Figs. 7d to 7a display a series of secondary twinning which generates nanotwins in the microtwin, and finally forms a hierarchically twinned microstructure. The secondary twinning is subject to a pair of conjugated twinning systems[‡]. These two systems for the secondary twinning (still represented by K_1, η_1 for simplicity) corresponds to: $(1\ 1\ 2)[1\ 1\ \bar{1}]$ and $(\bar{1}\ \bar{1}\ 2)[1\ 1\ 1]$ (Fig. 7d). From Figs. 7d to 7c, the conjugated twinning systems operate respectively on the two twin domains A, B in the already formed microtwin, cause their internal twinning, and generate the martensitic variant pair A–B. Still this pair of conjugated twinning systems, if both operate on a single twin domain (e.g., B in Fig. 7d) of the microtwin A–B, will create the internally twinned variant pair B–C (or A–D). At the same time, a single twinning system $(1\ 1\ 2)[1\ 1\ \bar{1}]$ operates on both domains of the microtwin, causes their internal twinning likewise, and produces the martensitic variant pair A–C.

All the above twinning systems are depicted in Fig. S5 for the convenience of directly viewing their geometric relationships. A detailed process of deriving those twinning systems is given in the supplementary material (Section 3). In addition, by analyzing Fig. S5, a common lattice direction along which the nanotwin boundaries in both variants A and B are edge-on can be predicted (though this common direction shared by A, B was not found in our experiments), which is explained in the supplementary material (Section 4).

[‡] If a twinning system is defined by its four twinning elements: (K_1, η_1, K_2, η_2), then the indices in a conjugated twinning system are (K_2, η_2, K_1, η_1) [24]

4.2.2. Explanation of the deformations in an NM martensitic plate group

Generally speaking, during the deformation of a nanotwin system under a proper external stress, the twin domains with a favorable orientation relative to the applied stress will grow at the expense of the other domains [13-18]. This transition between twin domains occurs through a purely twinning/detwinning process which necessitates a perfect {1 1 2} twin relationship [20]. Nevertheless, the inter-variant lamellae are not perfectly or even not twin-related at all when $\lambda > 0$ (Table 3). Moreover, the inter-variant interfaces may have a high density of defects and are often considered as immobile [25, 27] (though their short-range motion about 100 nm may happen occasionally [14]). For above-mentioned reasons, our geometric model does not consider the motion of inter-variant interfaces when $\lambda > 0$. Therefore, the deformation occurred in an NM martensitic plate group starts from twinning/detwinning of the inner-variant nanotwins (i.e., lamellae I–II, III–IV, and V–VI in Fig. 7), and then by analyzing the model, many deformation phenomena of the NM martensites can be reasonably explained.

In the variant pair A–B, there are only three possible deformation paths. a) In both variants, the major lamellae grow at the expense of the minor ones. b) Still in both variants, the minor lamellae grow at the expense of the major ones. c) In one variant the case a) operates, while in another the case b) operates.

In the first two cases, crystal rotations will occur not only to reduce the interfacial energy but also to accommodate the variation of defect density in the interfaces. Either the major lamellae in case a) or the minor ones in case b) can grow and form a microtwin and eventually evolve into a single crystal. However, the significant difference between these two cases lies in the way how a single crystal is produced.

In case a), the initial major–major lamellae across the inter-variant interface approach to a twin relationship (type **ii** OR in Table 3). After the major lamellae in both variants grow from nanotwins into a microtwin, one twin domain in the newly formed microtwin grows at the expense of the other domain (like the domain growth in nanotwins), which eventually leads to the formation of a single crystal. From Figs. 7a to 7e shows a complete deformation path in the case a).

In case b), the initial minor–minor lamellae across the inter-variant interface are not twin-related (type **i** OR in Table 3). With the domain growth in nanotwins, the growing minor lamellae accompanied by crystal rotation will form two variants with an identical orientation, which then naturally merge into a single crystal.

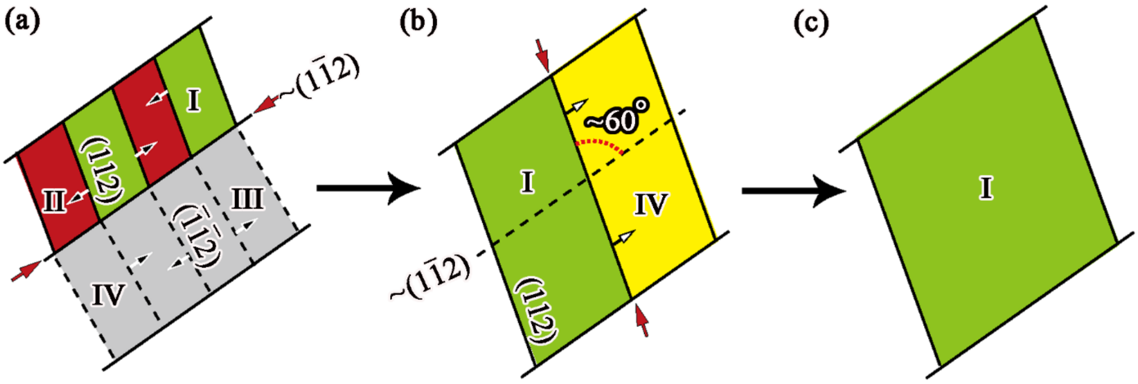

Fig. 8. A schematic showing the deformation path of the case c).

In case c), its deformation path can also be deduced from Fig. 7. For clarity, it is drawn in an individual figure (Fig. 8). Like the cases a) and b), the first step of case c) is domain growth in the nanotwins by means of twinning/detwinning. The initial orientation of A–B interface is close to the $(1\ \bar{1}\ 2)$ plane of the major lamellae (Fig. 8a). After the first step, the A–B variant pair grows into a microtwin, and the orientation of its interface (twin boundary) becomes parallel to the (1 1 2) twinning plane of the nanotwins (Fig. 8b). This reorientation of the A–B interface needs a large crystal rotation (about 60°), which implies the improbability of the deformation path in case c) to form a single crystal.

The deformation paths of the variant pair A–C are the same as those of A–B, due to their crystallographic similarity (Table 3). For the same crystallographic reason demonstrated in Table 3, the variant pair B–C also has deformation paths similar to A–B. The only difference lies in the fact that, because the major–major and minor–minor lamellae in the variant pair B–C have exactly the same OR type, both cases a) and b) for this variant pair share a same way to form a single crystal (i.e., via crystal merging incurred by their identical orientation, as illustrated from Figs. 7c to 7d).

The above deformation paths deduced from the geometric model (Fig. 7) for different variant pairs in an NM martensitic plate group can be substantiated by many reported experimental results. For the variant pairs A–B and A–C, their deformation path in case a) was supported by the work observed by Zárubová et al. [13], and their case b) was reported by Dai et al. [17]. For the variant pair A–D (or B–C), its two deformation paths in cases a) and b) were both verified by Szczerba and Chulist [15]. Unsurprisingly, there is no convincing experimental evidence hitherto that can validate the deformation path described in case c).

So far the deformation of NM martensites is still an open topic, and new deformation phenomena are expected to be observed. To completely clarify all deformation phenomena happened in the NM martensites, more knowledge about the characters of twinning dislocation, twinning stress, and interfacial defects is required. With the help of our geometric model, many current deformation phenomena of the NM martensites in Ni-Mn-Ga alloys can be rationally elucidated. The present results reported in this paper lay a foundation for further study on the NM martensites in MSMAs, including their interface structure, microscale deformation mechanism, as well as MFIS improvement.

5. Conclusions

This paper systematically determines the ORs between the nanoscale lamellae in an NM martensitic plate group with a special emphasis on the A–B type variant pair. Inside an individual variant, all lamellae are nanotwins. Across the inter-variant interfaces, the ORs between all major–major, minor–minor, and major–minor lamellae in the three martensitic variant pairs A–B, A–C, A–D (or B–C) can be classified into three crystallographic characteristics:

i. a simple rotation (< 25°) without {1 1 2} twin relationship.

ii. $(1\ \bar{1}\ 2)$ twinning operation plus a small (< 12°) rotation, with the twinning plane nearly parallel to the inter-variant interface.

iii. (1 1 2) or $(\bar{1}\ \bar{1}\ 2)$ twinning operation plus a rotation (< 25°), with the twinning plane exactly parallel to the inner-variant nanotwin boundary.

By integrating both experimental observations and theoretical calculations, a geometric model for a whole NM martensitic plate group is established, in order that:

- The twinning systems with a hierarchically twinned microstructure be clarified.
- The formation mechanisms that underlie different variant pairs be revealed.
- The deformation paths in an NM martensitic plate group be explained.

Acknowledgements

The authors would like to acknowledge the financial support of the 111 Project (B08040) of China, the Natural Science Foundation of China (grant No. 51071125, 51271147, 51201134 and 51201135), the Major Project of Natural Science Foundation of Jiangxi Province (grant No. 20161ACB20010), the Hong Kong Research Grants Council through the Early Career Scheme (project No. 25301617), and the Hong Kong Polytechnic University grant (project No. 1-ZE6G).

References

[1] O. Söderberg, Y. Ge, A. Sozinov, S.P. Hannula, V.K. Lindroos, Recent breakthrough development of the magnetic shape memory effect in Ni–Mn–Ga alloys, Smart Mater. Struct., 14(5) (2005) S223-S235.

[2] J. Mohd Jani, M. Leary, A. Subic, M.A. Gibson, A review of shape memory alloy research, applications and opportunities, Mater. Design, 56 (2014) 1078-1113.

[3] E. Pagounis, R. Chulist, M.J. Szczerba, M. Laufenberg, Over 7% magnetic field-induced strain in a Ni–Mn–Ga five-layered martensite, Appl. Phys. Lett., 105(5) (2014) 052405.

[4] E. Pagounis, M.J. Szczerba, R. Chulist, M. Laufenberg, Large magnetic field-induced work output in a NiMnGa seven-layered modulated martensite, Appl. Phys. Lett., 107(15) (2015) 152407.

[5] A. Sozinov, N. Lanska, A. Soroka, W. Zou, 12% magnetic field-induced strain in Ni–Mn–Ga-based non-modulated martensite, Appl. Phys. Lett., 102(2) (2013) 021902.

[6] V.A. Chernenko, M. Chmielus, P. Müllner, Large magnetic-field-induced strains in Ni–Mn–Ga nonmodulated martensite, Appl. Phys. Lett., 95(10) (2009) 104103.

[7] A. Çakır, L. Righi, F. Albertini, M. Acet, M. Farle, S. Aktürk, Extended investigation of intermartensitic transitions in Ni–Mn–Ga magnetic shape memory alloys: A detailed phase diagram determination, J. Appl. Phys., 114(18) (2013) 183912.

[8] P. Müllner, A.H. King, Deformation of hierarchically twinned martensite, Acta Mater., 58(16) (2010) 5242-5261.

[9] S. Kaufmann, R. Niemann, T. Thersleff, U.K. Rößler, O. Heczko, J. Buschbeck, B. Holzapfel, L. Schultz, S. Fähler, Modulated martensite: why it forms and why it deforms easily, New J. Phys., 13(5) (2011) 053029.

[10] K. Otsuka, C.M. Wayman. Shape memory materials. Cambridge: Cambridge University Press; 1998. p. 18-21.

[11] J.M. Ball, R.D. James, Fine phase mixtures as minimizers of energy, Arch. Rat. Mech. Anal, 100 (1987) 13-52.

[12] K. Bhattacharya, Wedge-like microstructure in martensites, Acta metall. mater., 39(10) (1991) 2431-2444.

[13] N. Zárubová, Y. Ge, O. Heczko, S.P. Hannula, In situ TEM study of deformation twinning in Ni–Mn–Ga non-modulated martensite, Acta Mater., 61(14) (2013) 5290-5299.

[14] B. Muntifering, L. Kovarik, N.D. Browning, R.C. Pond, W.B. Knowlton, P. Müllner, Stress-assisted removal of conjugation boundaries in non-modulated Ni–Mn–Ga by coordinated secondary twinning, J. Mater. Sci., 51(1) (2015) 457-466.

[15] M.J. Szczerba, R. Chulist, Detwinning of a non-modulated Ni–Mn–Ga martensite: From self-accommodated microstructure to single crystal, Acta Mater., 85 (2015) 67-73.

[16] L. Hou, Y. Dai, Y. Fautrelle, Z. Li, Z. Ren, C. Esling, X. Li, Detwinning of hierarchically structured martensitic variants in a directionally solidified non-modulated Ni–Mn–Ga alloy under uniaxial loading, Scr. Mater., 134 (2017) 85-90.

[17] Y. Dai, L. Hou, Y. Fautrelle, Z. Li, C. Esling, Z. Ren, X. Li, Detwinning process of martensite in $Ni_{58}Mn_{25}Ga_{17}$ as a high temperature shape memory alloy under uniaxial compression, Int. J. Plast., 103 (2018) 203-213.

[18] Y. Ge, N. Zárubová, O. Heczko, S.P. Hannula, Stress-induced transition from modulated 14M to non-modulated martensite in Ni–Mn–Ga alloy, Acta Mater., 90 (2015) 151-160.

[19] R. Chulist, M. Faryna, M.J. Szczerba, Orientation relationship between austenite and non-modulated martensite in Ni–Mn–Ga single crystals, Acta Mater., 103 (2016) 836-843.

[20] R.C. Pond, B. Muntifering, P. Müllner, Deformation twinning in Ni_2MnGa, Acta Mater., 60(9) (2012) 3976-3984.

[21] D.Y. Cong, Y.D. Zhang, C. Esling, Y.D. Wang, J.S. Lecomte, X. Zhao, L. Zuo, Microstructural and crystallographic characteristics of interpenetrating and non-interpenetrating multiply twinned nanostructure in a Ni–Mn–Ga ferromagnetic shape memory alloy, Acta Mater., 59(18) (2011) 7070-7081.

[22] Z. Li, N. Xu, Y. Zhang, C. Esling, J.-M. Raulot, X. Zhao, L. Zuo, Composition-dependent ground state of martensite in Ni–Mn–Ga alloys, Acta Mater., 61(10) (2013) 3858-3865.

[23] B. Yang, Z.B. Li, Y.D. Zhang, G.W. Qin, C. Esling, O. Perroud, X. Zhao, L. Zuo, Microstructural features and orientation correlations of non-modulated martensite in Ni–Mn–Ga epitaxial thin films, Acta Mater., 61(18) (2013) 6809-6820.

[24] B. Muntifering, R.C. Pond, L. Kovarik, N.D. Browning, P. Müllner, Intra-variant substructure in Ni–Mn–Ga martensite: Conjugation boundaries, Acta Mater., 71 (2014) 255-263.

[25] B. Reinholz, S. Brinckmann, A. Hartmaier, B. Muntifering, W.B. Knowlton, P. Müllner, Influence of the twin microstructure on the mechanical properties in magnetic shape memory alloys, Acta Mater., 108 (2016) 197-206.

[26] S. Ouyang, Y.Q. Yang, M. Han, Z.H. Xia, B. Huang, X. Luo, G.M. Zhao, W. Zhang, Twin relationships between nanotwins inside A–C type variant pair in Ni–Mn–Ga alloy, Acta Mater., 84 (2015) 484-496.

[27] S. Ouyang, Y.Q. Yang, M. Han, Z.H. Xia, B. Huang, X. Luo, G.M. Zhao, Y.X. Chen, Structure of A–C type intervariant interface in nonmodulated martensite in a Ni–Mn–Ga alloy, ACS Appl. Mater. Interfaces, 8(26) (2016) 16985-16996.

[28] P.J. Webster, K.R.A. Ziebeck, S.L. Town, M.S. Peak, Magnetic order and phase transformation in Ni_2MnGa, Philos. Mag. B, 49(3) (1984) 295-310.

[29] M. Han, J.C. Bennett, M.A. Gharghouri, J. Chen, C.V. Hyatt, N. Mailman, Microstructure characterization of the non-modulated martensite in Ni–M–Ga alloy, Mater. Charact., 59(6) (2008) 764-768.

[30] D.Y. Cong, Y.D. Zhang, Y.D. Wang, M. Humbert, X. Zhao, T. Watanabe, L. Zuo, C. Esling, Experiment and theoretical prediction of martensitic transformation crystallography in a Ni–Mn–Ga ferromagnetic shape memory alloy, Acta Mater., 55(14) (2007) 4731-4740.

[31] X. Zhang, P.M. Kelly, A. Atrens, A new metastable orthorhombic phase Cu_9Y, Acta Metall. Mater., 41(10) (1993) 2877-2885.

[32] L. Straka, O. Heczko, H. Seiner, N. Lanska, J. Drahokoupil, A. Soroka, S. Fähler, H. Hänninen, A. Sozinov, Highly mobile twinned interface in 10M modulated Ni–Mn–Ga martensite: Analysis beyond the tetragonal approximation of lattice, Acta Mater., 59(20) (2011) 7450-7463.

[33] T. Inamura, H.Y. Kim, H. Hosoda, S. Miyazaki, Competition between invariant habit plane and compatible junction plane in TiNb-based shape memory alloy, J. Alloy. Compd., 577 (2013) S92-S95.